bioRxiv preprint doi: https://doi.org/10.1101/2022.03.17.480842; this version posted March 19, 2022. The copyright holder for this preprint (which was not certified by peer review) is the author/funder, who has granted bioRxiv a license to display the preprint in perpetuity. It is made available under aCC-BY 4.0 International license.

Ubiquitous lognormal distribution of neuron densities across mammalian cerebral cortex

Aitor Morales-Gregorio,[1,2,*,†] Alexander van Meegen,[1,2,*] Sacha J. van Albada[1,2]

[1]Institute of Neuroscience and Medicine (INM-6) and Institute for Advanced Simulation (IAS-6) and JARA-Institut Brain Structure-Function Relationships (INM-10), Jülich Research Centre, Jülich, Germany

[2]Institute of Zoology, University of Cologne, Cologne, Germany

∗These authors contributed equally to this work.

†To whom correspondence should be addressed; e-mail: a.morales-gregorio@fz-juelich.de

Abstract

Numbers of neurons and their spatial variation are fundamental organizational features of the brain. Despite the large corpus of data available in the literature, the statistical distributions of neuron densities within and across brain areas remain largely uncharacterized. Here, we show that neuron densities are compatible with a lognormal distribution across cortical areas in several mammalian species. We find that this also holds true for uniformly sampled regions across cortex as well as within cortical areas. Our findings uncover a new organizational principle of cortical cytoarchitecture. The ubiquitous lognormal distribution of neuron densities adds to a long list of lognormal variables in the brain.

bioRxiv preprint doi: https://doi.org/10.1101/2022.03.17.480842; this version posted March 19, 2022. The copyright holder for this preprint (which was not certified by peer review) is the author/funder, who has granted bioRxiv a license to display the preprint in perpetuity. It is made available under aCC-BY 4.0 International license.

Introduction

Neurons are not uniformly distributed across the cerebral cortex; their density varies strongly across areas and layers [1]. The neuron density directly affects short-range as well as long-range neuronal connectivity [2, 3]. Elucidating the distribution of neuron densities across the brain therefore provides insight into its connectivity structure and, ultimately, cognitive function. Additionally, statistical distributions are essential for the construction of computational models, which rely on predictive relationships and organizational principles where the experimental data are missing [4, 5]. Previous quantitative studies have provided reliable estimates for cell densities across the cerebral cortex of rodents [6, 7, 8], non-human primates [8, 9, 10, 11, 12, 13], large carnivores [14], and humans [15, 1]. However, to the best of our knowledge, the univariate distribution of neuron densities across and within cortical areas has not yet been statistically characterized. Instead, most studies focus on qualitative and quantitative comparisons across species, areas, or cortical layers. Capturing the entire distribution is necessary because long-tailed, highly skewed distributions are prevalent in the brain [16] and invalidate the intuition—guided by the central limit theorem—that the vast majority of values are in a small region of a few standard deviations around the mean.

Here, we for the first time characterize the distribution of neuron densities ρ across mammalian cerebral cortex. Based on the sample histograms (Figure 1) we hypothesize that ρ follows a lognormal distribution, similar to many other neuroanatomical and physiological variables such as synaptic strengths, axonal widths, and cortico-cortical connection densities [16, 17, 18]. Using neuron density data from mouse (*Mus musculus*), marmoset (*Callithrix jacchus*), macaque (*Macaca mulatta*), human (*Homo sapiens*), galago (*Otolemur garnettii*), owl monkey (*Aotus nancymaae*), and baboon (*Papio cynocephalus anubis*) we confirm this hypothesis for the given species (see Cell density data for a detailed description of the data). Going

bioRxiv preprint doi: https://doi.org/10.1101/2022.03.17.480842; this version posted March 19, 2022. The copyright holder for this preprint (which was not certified by peer review) is the author/funder, who has granted bioRxiv a license to display the preprint in perpetuity. It is made available under aCC-BY 4.0 International license.

beyond the distribution across cortical areas, we furthermore show that neuron densities within most areas of marmoset cortex are also compatible with a lognormal distribution. Moreover, we show that the lognormal distribution can emerge during neurogenesis from a simple cell division model with variability. Finally, we compare with several other distributions and find that none outperform the lognormal distribution as a model of the data within and across cortex.

Results

To test for lognormality, we take the natural logarithm, $\ln(\rho)$, which converts lognormally distributed samples into normally distributed samples (Figure 1B). We then test for normality of $\ln(\rho)$ using the Shapiro-Wilk (SW) test, the most powerful among a number of commonly applied normality tests [19]. Large outliers (|z-scored $\ln(\rho)| \geq 3$; marked with a red cross in Figure 1C) were excluded from the normality test. The removed outliers are area $\mathrm{V1}$ in macaque and marmoset, which have densities far outside the range for all other areas in both species, and area APir in marmoset, which has a noticeably distinct cytoarchitecture with respect to the rest of the cerebral cortex [9]. We denote different data sets for the same species with subscript indices (see Cell density data). The SW test concludes that the normality hypothesis of $\ln(\rho)$ cannot be rejected for mouse, marmoset, macaque$_1$, human, galago$_1$, owl monkey, and baboon (see Figure 1B). For the data sets macaque$_2$ and galago$_2$ the normality hypothesis is rejected ($p < 0.05$); however, in these data sets, the densities were sampled neither uniformly nor based on a cytoarchitectonic parcellation. The normality hypothesis for the distribution across cytoarchitectonic areas is further supported by Figure 1C, which shows that the relation between theoretical quantiles and ordered samples is almost perfectly linear except for macaque$_2$ and galago$_2$. Next, we test the z-scored $\ln(\rho)$ from the different species and data sets against each other and find that they are pairwise statistically indistinguishable ($\alpha = 0.05$ level; two-sample two-sided Kolmogorov-Smirnov test, see Figure S1 for full test results).

bioRxiv preprint doi: https://doi.org/10.1101/2022.03.17.480842; this version posted March 19, 2022. The copyright holder for this preprint (which was not certified by peer review) is the author/funder, who has granted bioRxiv a license to display the preprint in perpetuity. It is made available under aCC-BY 4.0 International license.

Additionally, we control for cell types in the distributions of the mouse, galago$_1$, owl monkey, and baboon data. In the mouse data, different types of neurons and glia were labeled with specific genetic markers and their respective densities were reported separately for all cell types [7]. In the galago$_1$, owl monkey, and baboon data sets, the total numbers of cells and neurons were reported separately [11]. We show that all subtypes of neurons in the mouse are compatible with a lognormal distribution (Figure S2; SW test on $\ln(\rho)$, $p > 0.05$) while glia are not—with the notable exception of oligodendrocytes. When neurons and glia are pooled together (Figure S2C,D), the distribution of $\ln(\rho)$ still passes the SW normality test, likely due to the distribution being dominated by the neurons. Similar observations are made in the baboon data, where the glia do not pass the lognormality test, but the neurons do. In the cases of galago$_1$ and owl monkey both the neurons and glia pass the lognormality test (Figure S2), which may, however, be partly due to the small number of density samples (N=12 in both cases). Thus, the mouse and baboon data—with large samples sizes (N=42 and N=142, respectively)—suggest that it is the neuron densities that follow a lognormal distribution but not necessarily the glia densities.

Furthermore, we also perform a control test on the different types of staining—Nissl and NeuN—using the macaque$_1$ data. The staining methods differ in their treatment of glia: NeuN tends to label neuronal cell bodies only while Nissl indiscriminately labels both neurons and glia. We show that regardless of staining type the cell densities pass the lognormality test (Figure S3; SW test on $\ln(\rho)$ with $p > 0.05$), suggesting that counting some glia in the cell densities does not confound our analysis of the macaque$_1$ data.

Taken together, the normality test, the quantiles plots, the pairwise tests, the cell type comparison, and the staining method comparison provide compelling evidence that the logarithmized neuron densities are normally distributed across cytoarchitectonic areas. This also holds for uniformly sampled neuron densities (baboon) but not for a sampling that is neither uniform

bioRxiv preprint doi: https://doi.org/10.1101/2022.03.17.480842; this version posted March 19, 2022. The copyright holder for this preprint (which was not certified by peer review) is the author/funder, who has granted bioRxiv a license to display the preprint in perpetuity. It is made available under aCC-BY 4.0 International license.

nor based on a cytoarchitectonic parcellation (macaque$_2$, galago$_2$). Thus, the neuron densities are consistent with a lognormal distribution across the different cortical areas, as long as sampling is not irregular.

To investigate whether the lognormal distribution holds within cortical areas, we leverage numerical estimates of neuron density in marmoset [9]. Neurons were counted within $150 \times 150\ \mu m$ counting frames for four strips per cortical area, all originating from the same subject. The neuron densities within the counting frames ρ_s are the within-area samples; their sample distributions in three representative areas (MIP, V2, and V3; Figure 2A) again suggest a lognormal distribution. As before, we test for lognormality by testing $\ln(\rho_s)$ for normality with the SW-test (for full test results see Table S2). At significance level $\alpha = 0.05$, the normality hypothesis is not rejected for 86 out of 116 areas; whereas at $\alpha = 0.001$, this is the case for 112 out of 116 areas (Figure 2B,C). Thus, regardless of the precise significance threshold, the lognormality hypothesis cannot be rejected within most cortical areas in the marmoset cortex.

This finding raises the question how the intricate process of neurogenesis [20] culminates in lognormally distributed neuron densities in almost all areas. A simple model shows that there is no need for a specific regulatory mechanism: assuming that the proliferation of the neural progenitor cells is governed by a noisy rate

$$\lambda(t) = \mu(t) + \xi(t), \tag{1}$$

where $\mu(t)$ denotes the mean rate and $\xi(t)$ is a zero-mean Gaussian process, the resulting population of progenitor cells, and eventually neurons, is lognormally distributed (see Model of progenitor cell division with variability). Thus, the lognormal neuron density distribution within areas could be a hallmark of a cell division process with variability. The model furthermore predicts that the mean and variance of $\ln(\rho)$ increase with proliferation time. Since the proliferation time varies up to twofold between areas [20], mean and variance of $\ln(\rho)$ are correlated

bioRxiv preprint doi: https://doi.org/10.1101/2022.03.17.480842; this version posted March 19, 2022. The copyright holder for this preprint (which was not certified by peer review) is the author/funder, who has granted bioRxiv a license to display the preprint in perpetuity. It is made available under aCC-BY 4.0 International license.

across areas according to the model—indeed, they are significantly correlated in the marmoset data (Pearson $r = 0.32,\ p < 10^{-3}$, Figure S4).

To complement the statistical hypothesis tests on the logarithmic densities, we compared the lognormal model with six other statistical distributions based on the relative likelihood (see Statistical model comparison). We included statistical distributions with support in $\mathbb{R}^+$ since neuron densities cannot be negative: lognormal, truncated normal, inverse normal, gamma, inverse gamma, Lévy, and Weibull. Of those distributions the lognormal, inverse normal, and inverse gamma stand out as the distributions with the highest relative likelihoods, both across the entire cortex and within cortical areas (Figure S5A, Figure S6A). A visual inspection of the fitted distribution reveals that the lognormal, inverse normal, and inverse gamma produce virtually indistinguishable probability densities (Figure S5B, Figure S6C); indeed, the relative likelihoods of the three models are above 0.05 in all cases. This suggests that the data could theoretically be distributed according to either the lognormal, inverse normal, or inverse gamma distribution. However, out of these, the lognormal distribution could arise from a simple model of cell division (equation (1))—while no interpretable mechanisms leading to inverse normal or inverse gamma distributions are known in this context. Thus, the similar likelihood and a simple biophysical explanation together argue for a lognormal rather than an inverse normal or inverse gamma distribution of neuron densities.

Discussion

In conclusion, we show that neuron densities are compatible with a lognormal distribution across cortical areas in multiple mammalian cortices and within most cortical areas of the marmoset, uncovering a previously unexplored organizational principle of cerebral cortex. Furthermore, we propose a simple model, based on a cell division process of the progenitor cells with variability, that accounts for the emerging lognormal distributions within areas. Lastly, we show

bioRxiv preprint doi: https://doi.org/10.1101/2022.03.17.480842; this version posted March 19, 2022. The copyright holder for this preprint (which was not certified by peer review) is the author/funder, who has granted bioRxiv a license to display the preprint in perpetuity. It is made available under aCC-BY 4.0 International license.

that none of an extensive list of statistical models outperform the lognormal distribution. Our results are in agreement with the observation that surprisingly many characteristics of the brain follow lognormal distributions [16]. Moreover, this analysis highlights the importance of characterizing the statistical distributions of brain data because simple summary statistics—such as the mean or standard deviation—lack nuance and are not necessarily a good representation of the underlying distribution.

The distributions of neuron and cell densities in general depend on the underlying spatial sampling. We found that neuron densities follow a lognormal distribution within cytoarchitectonically defined areas, across such areas, and when averaged within small parcels uniformly sampled across cortex, but not when sampled in a highly non-uniform manner not following cytoarchitectonic boundaries. The observation of lognormality both within and across cytoarchitectonic areas as well as across small uniformly sized parcels suggests an interesting topic for further research: uncovering whether the neuron densities obey an invariance principle across scales.

In principle, cortex-wide organizational structures might be by-products of development or evolution that serve no computational function [21]—but the fact that we observe the same organizational principle for several species and across most cortical areas suggests that the lognormal distribution serves some purpose. Heterogeneous neuron densities could assist computation through their association with heterogeneity in other properties such as connectivity and neuronal time constants [4, 22]; indeed, such heterogeneity is known to be a valuable asset for neural computation [23, 24]. Alternatively, localized concentration of neurons in certain areas and regions could also serve a metabolic purpose [25], because centralization supports more efficient energy usage. This is particularly relevant since approximately half of the brain's energy consumption is used to support the communication between neurons [26]. Also from the perspective of cortical hierarchies it makes sense to have few areas with high neuron densities

bioRxiv preprint doi: https://doi.org/10.1101/2022.03.17.480842; this version posted March 19, 2022. The copyright holder for this preprint (which was not certified by peer review) is the author/funder, who has granted bioRxiv a license to display the preprint in perpetuity. It is made available under aCC-BY 4.0 International license.

and many areas with lower neuron densities: Low-density areas contain neurons with large dendritic trees [27] receiving convergent inputs from many neurons in high-density areas lower in the hierarchy. The neurons with extensive dendritic trees in higher areas are involved in different, area-specific abstractions of the low-level sensory information [28, 29]. There is probably not a single factor that leads to lognormal neuron densities in the cortex; further research will be needed to refine our findings and uncover the functional implications.

References

[1] C. von Economo, G. N. Koskinas, L. C. Triarhou, *Atlas of Cytoarchitectonics of the Adult Human Cerebral Cortex* (Karger, 2008).

[2] V. Braitenberg, A. Schüz, *Anatomy of the Cortex: Statistics and Geometry* (Springer-Verlag, Berlin, Heidelberg, New York, 1991).

[3] M. Ercsey-Ravasz, *et al.*, *Neuron* **80**, 184 (2013).

[4] C. C. Hilgetag, S. F. Beul, S. J. van Albada, A. Goulas **3**, 905 (2019).

[5] S. J. van Albada, *et al.*, *arXiv* (2020).

[6] S. Herculano-Houzel, C. Watson, G. Paxinos, *Frontiers in Neuroanatomy* **7** (2013).

[7] C. Erö, M.-O. Gewaltig, D. Keller, H. Markram, *Frontiers in Neuroinformatics* **12**, 84 (2018).

[8] C. J. Charvet, D. J. Cahalane, B. L. Finlay, *Cerebral Cortex* **25**, 147 (2015).

[9] N. Atapour, *et al.*, *Cerebral cortex* **29**, 3836 (2019).

[10] S. F. Beul, C. C. Hilgetag, *NeuroImage* **189**, 777 (2019).

bioRxiv preprint doi: https://doi.org/10.1101/2022.03.17.480842; this version posted March 19, 2022. The copyright holder for this preprint (which was not certified by peer review) is the author/funder, who has granted bioRxiv a license to display the preprint in perpetuity. It is made available under aCC-BY 4.0 International license.

[11] C. E. Collins, D. C. Airey, N. A. Young, D. B. Leitch, J. H. Kaas, *Proceedings of the National Academy of Sciences* **107**, 15927 (2010).

[12] C. E. Collins, *et al.*, *Proceedings of the National Academy of Sciences* **113**, 740 (2016).

[13] E. C. Turner, *et al.*, *Brain, Behavior and Evolution* **88**, 1 (2016).

[14] D. Jardim-Messeder, *et al.*, *Frontiers in Neuroanatomy* **11**, 118 (2017).

[15] C. S. von Bartheld, J. Bahney, S. Herculano-Houzel, *Journal of Comparative Neurology* **524**, 3865 (2016).

[16] G. Buzsáki, K. Mizuseki, *Nature Reviews Neuroscience* **15**, 264 (2014).

[17] N. T. Markov, *et al.*, *Cerebral Cortex* **24**, 17 (2014).

[18] P. A. Robinson, X. Gao, Y. Han, *Biological Cybernetics* **115**, 121 (2021).

[19] N. M. Razali, B. W. Yap, *Journal of Statistical Modeling and Analytics* **2**, 21 (2011).

[20] P. Rakic, *Nature Reviews Neuroscience* **3**, 65 (2002).

[21] A. G. Otopalik, A. C. Sutton, M. Banghart, E. Marder, *eLife* **6**, e23508 (2017).

[22] W. Rall, *Biophysical Journal* **9**, 1483 (1969).

[23] R. Duarte, A. Morrison, *PLOS Computational Biology* **15**, e1006781 (2019).

[24] N. Perez-Nieves, V. C. H. Leung, P. L. Dragotti, D. F. M. Goodman, *Nature Communications* **12**, 5791 (2021).

[25] M. Bélanger, I. Allaman, P. Magistretti, *Cell Metabolism* **14**, 724 (2011).

[26] S. B. Laughlin, T. J. Sejnowski, *Science* **301**, 1870 (2003).

bioRxiv preprint doi: https://doi.org/10.1101/2022.03.17.480842; this version posted March 19, 2022. The copyright holder for this preprint (which was not certified by peer review) is the author/funder, who has granted bioRxiv a license to display the preprint in perpetuity. It is made available under aCC-BY 4.0 International license.

[27] G. N. Elston, M. Rosa, *Cerebral Cortex* **8**, 278 (1998).

[28] S. Kumar, K. E. Stephan, J. D. Warren, K. J. Friston, T. D. Griffiths, *PLoS Computational Biology* **3**, e100 (2007).

[29] S. L. Brincat, M. Siegel, C. von Nicolai, E. K. Miller, *Proceedings of the National Academy of Sciences* **115** (2018).

[30] E. S. Lein, *et al.*, *Nature* **445**, 168 (2007).

[31] H. W. Dong, *The Allen reference atlas: A digital color brain atlas of the C57Bl/6J male mouse.* (John Wiley & Sons inc., 2008).

[32] G. Paxinos, C. R. R. Watson, M. Petrides, M. G. Rosa, H. Tokuno, *The Marmoset Brain in Stereotaxic Coordinates* (2012).

[33] N. G. Van Kampen, *Stochastic Processes in Physics and Chemistry* (North Holland, 2007), third edn.

[34] C. A. Braumann, *Mathematical Biosciences* **206**, 81 (2007).

Acknowledgements

We thank Günther Palm for useful discussions, Alexandre René for useful discussions and help with the Bayesian model comparison, Anno Kurth for discussions about geometric Brownian motion, and Jon Martinez Corral for proofreading an early draft. **Funding:** This work was supported by the European Union Horizon 2020 Framework Programme for Research and Innovation (Human Brain Project SGA2 grant number 785907 and HBP SGA3 grant number 945539) and the Deutsche Forschungsgemeinschaft (DFG, German Research Foundation) under Priority Program (SPP 2041 ”Computational Connectomics”) [S.J. van Albada: AL 2041/1-1 and

bioRxiv preprint doi: https://doi.org/10.1101/2022.03.17.480842; this version posted March 19, 2022. The copyright holder for this preprint (which was not certified by peer review) is the author/funder, who has granted bioRxiv a license to display the preprint in perpetuity. It is made available under aCC-BY 4.0 International license.

2041/1-2] and Open Access Publication Costs grant 491111487. **Author contributions:** Conceptualization AMG, AvM, SvA; Data curation AMG; Formal Analysis AMG, AvM; Funding acquisition SvA; Investigation AMG, AvM, SvA; Methodology AMG, AvM, SvA; Project administration SvA; Resources SvA; Software AMG, AvM; Supervision SvA; Validation AvM; Visualization AMG; Writing - original draft AMG, AvM; Writing – review & editing AMG, AvM, SvA. **Competing interests:** The authors declare no competing interests. **Data and materials availability:** This work produced no new data and instead relied on a corpus of neuron density data available from the literature, which we gratefully acknowledge; see Cell density data for a detailed description.

bioRxiv preprint doi: https://doi.org/10.1101/2022.03.17.480842; this version posted March 19, 2022. The copyright holder for this preprint (which was not certified by peer review) is the author/funder, who has granted bioRxiv a license to display the preprint in perpetuity. It is made available under aCC-BY 4.0 International license.

Figures

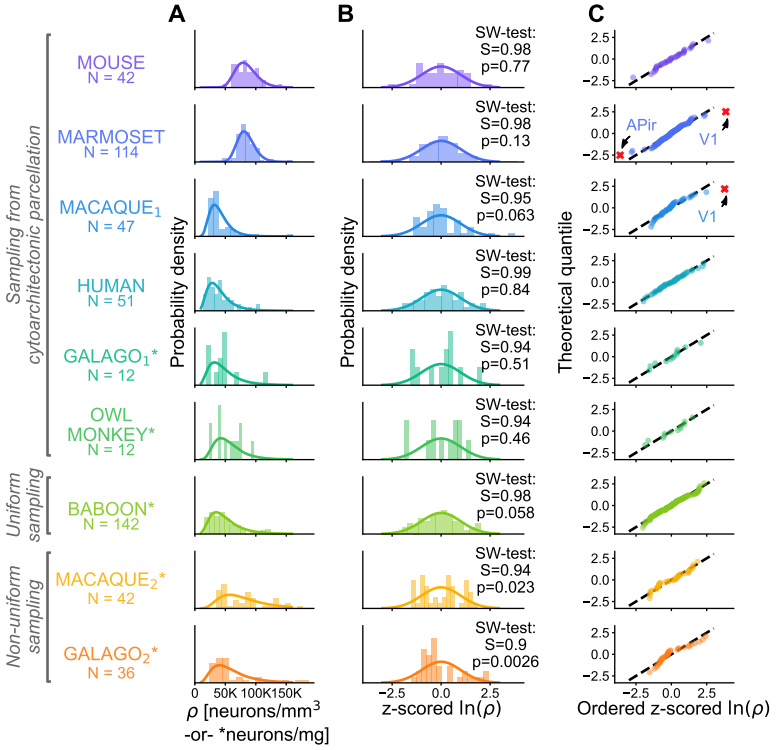

Figure 1: Neuron and cell densities ρ follow a lognormal distribution across cortical areas for multiple species. **A** Histogram of ρ (bars) and probability density function of a fitted lognormal distribution (line). **B** Z-scored $\ln(\rho)$ histogram (bars), standard normal distribution (line), and result of the Shapiro-Wilk normality test. **C** Probability plot of z-scored $\ln(\rho)$. Discarded outliers marked with a red cross.

bioRxiv preprint doi: https://doi.org/10.1101/2022.03.17.480842; this version posted March 19, 2022. The copyright holder for this preprint (which was not certified by peer review) is the author/funder, who has granted bioRxiv a license to display the preprint in perpetuity. It is made available under aCC-BY 4.0 International license.

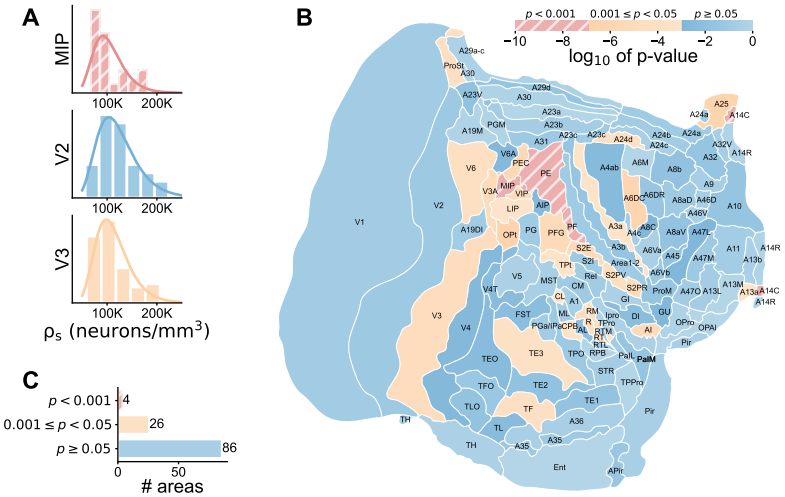

Figure 2: Neuron densities ρ_s follow a lognormal distribution within most areas of marmoset cortex. **A** Sample histograms of ρ_s and fitted lognormal distributions for three areas representing different degrees of lognormality. **B** Log_{10} of p-value of Shapiro-Wilk normality test of $\ln(\rho_s)$ on a flattened representation of the marmoset cortex [9]. **C** Number of areas with p-values in the given significance ranges.

bioRxiv preprint doi: https://doi.org/10.1101/2022.03.17.480842; this version posted March 19, 2022. The copyright holder for this preprint (which was not certified by peer review) is the author/funder, who has granted bioRxiv a license to display the preprint in perpetuity. It is made available under aCC-BY 4.0 International license.

Materials and methods

Cell density data

Estimates of neuron density for the available cortical areas across the mouse (*Mus musculus*), marmoset (*Callithrix jacchus*), macaque (*Macaca mulatta*), human (*Homo sapiens*), galago (*Otolemur garnettii*), owl monkey (*Aotus nancymaae*), and baboon (*Papio cynocephalus anubis*) cerebral cortex were used in this study.

In the cases of mouse, marmoset, macaque$_1$, human, galago$_1$, and owl monkey the data were sampled from standard cytoarchitectonic parcellations; abbreviated names for all areas are listed in Table S1. Note that we use subscript indices to distinguish between different data sets on the same model animal, e.g. macaque$_1$ and macaque$_2$.

Neuron density estimates for the mouse were published in [7], and were measured from Nissl-body-stained slices, where genetic markers were used to distinguish between cell types. The data were provided in the Allen Brain Atlas parcellation [30, 31].

Neuron density estimates for the marmoset cortex were published in [9], and were measured from NeuN-stained slices. The data were provided in the Paxinos parcellation [32]. Neuron densities within each counting frame used in the original publication [9] (their Figure S1) were obtained via personal communication with Nafiseh Atapour, Piotr Majka, and Marcello G. Rosa.

The neuron density estimates in the first macaque data set, macaque$_1$, were previously published in visual form in [10], and were obtained from both Nissl-body- and NeuN-stained brain slices. Counts based on Nissl-body staining were scaled according to a linear relationship with the counts from NeuN staining obtained from selected areas where both types of data were available [10]. The data follow the M132 parcellation [17] and numerical values were provided by Sarah F. Beul and Claus C. Hilgetag via personal communication.

Cell density estimates for the human cortex were previously published in [1], and were

bioRxiv preprint doi: https://doi.org/10.1101/2022.03.17.480842; this version posted March 19, 2022. The copyright holder for this preprint (which was not certified by peer review) is the author/funder, who has granted bioRxiv a license to display the preprint in perpetuity. It is made available under aCC-BY 4.0 International license.

measured from Nissl-body-stained brain slices. The human data therefore most likely reflect combined neuron and glia densities. The data were provided in the von Economo parcellation [1].

Cell and neuron density estimates for galago$_{1\&2}$, owl monkey, baboon, and macaque$_2$ were previously published in [11], and were measured using the isotropic fractionator method. The data are sampled from common parcellation schemes in galago$_1$ and owl monkey, approximately equal-size samples in the baboon, and irregular non-uniform samples in macaque$_2$ and galago$_2$.

Statistical model comparison

In order to assess which model is most compatible with the data, we compared the relative likelihood of different distributions against each other. We included an extensive list of distributions with support on $\mathbb{R}^+$, estimated the distributions' parameters using maximum likelihood, and calculated the Akaike Information Criterion (AIC)

$$AIC = 2k - 2\ln\mathcal{L} \tag{2}$$

where k is the number of estimated parameters of the model and $\mathcal{L}$ is the estimated maximum likelihood. We further compare the models using the relative likelihood ($\mathcal{L}_r$)

$$\mathcal{L}_r = e^{(AIC_{\min} - AIC_i)/2} \tag{3}$$

where $AIC_{\min}$ is the minimum AIC across all models and AIC_i is the AIC for the ith model. Note that the relative likelihood is equal to the relative likelihood if the number of estimated parameters is the same in both models. The relative likelihood indicates the probability that, from among the tested models, the ith model most strongly limits the information loss. We take a significance threshold of $\alpha = 0.05$ on the relative likelihood to determine whether a model is significantly worse than the best possible model.

bioRxiv preprint doi: https://doi.org/10.1101/2022.03.17.480842; this version posted March 19, 2022. The copyright holder for this preprint (which was not certified by peer review) is the author/funder, who has granted bioRxiv a license to display the preprint in perpetuity. It is made available under aCC-BY 4.0 International license.

Model of progenitor cell division with variability

We assume that the proliferation of the neural progenitor cells is governed by a noisy rate

$$\lambda(t) = \mu_{\text{rate}} + \sigma_{\text{rate}}\xi(t), \tag{4}$$

where μ_{rate} denotes the mean rate, $\xi(t)$ is a zero-mean Gaussian white noise process, and σ_{rate} controls the strength of the noise. During proliferation, we assume that the population size of the progenitor cells grows exponentially with rate λ, i.e., it obeys $\frac{d}{dt}N = \lambda N$. Dividing by a reference volume and inserting equation (4), we obtain a stochastic differential equation (SDE) for the density of progenitor cells ρ:

$$\frac{d}{dt}\rho = (\mu_{\text{rate}} + \sigma_{\text{rate}}\xi(t))\rho \tag{5}$$

We here use the Stratonovich interpretation, i.e., we assume that the noise process has a small but finite correlation time before taking the white-noise limit [33].

Working in the Stratonovich interpretation, we can transform the SDE to $\frac{d}{dt}\ln\rho = \mu_{\text{rate}} + \sigma_{\text{rate}}\xi(t)$ with the solution [34]

$$\ln\rho(t) = \ln\rho_0 + \mu_{\text{rate}}t + \sigma_{\text{rate}}\int_0^t \xi(s)ds. \tag{6}$$

Since $\xi(t)$ is Gaussian and equation (6) is linear, $\ln\rho(t)$ is Gaussian and hence $\rho(t)$ is lognormally distributed. The parameters of this lognormal distribution are $\mu(t) = \langle\ln\rho(t)\rangle$ and $\sigma^2(t) = \langle\Delta(\ln\rho(t))^2\rangle$. Using equation (6), $\langle\xi(s)\rangle = 0$, and $\langle\xi(s)\xi(s')\rangle = \delta(s-s')$, we obtain [34]

$$\mu(t) = \ln\rho_0 + \mu_{\text{rate}}t \qquad \text{and} \qquad \sigma^2(t) = \sigma^2_{\text{rate}}t. \tag{7}$$

Thus, the neuron densities resulting from the model of cell division with variability, equation (5), are lognormally distributed with parameters $\mu(t)$ and $\sigma^2(t)$ specified in equation (7). In particular, equation (7) predicts that both parameters increase with the proliferation time t.

bioRxiv preprint doi: https://doi.org/10.1101/2022.03.17.480842; this version posted March 19, 2022. The copyright holder for this preprint (which was not certified by peer review) is the author/funder, who has granted bioRxiv a license to display the preprint in perpetuity. It is made available under aCC-BY 4.0 International license.

The model can be generalized while still leading to a lognormal distribution of neuron densities: 1) The mean rate can be time-dependent, $\mu_{\text{rate}} = \mu_{\text{rate}}(t)$. 2) The noise process can be an arbitrary zero-mean (a non-zero mean can always be incorporated into $\mu_{\text{rate}}(t)$) Gaussian process with correlation function $C_\xi(t, t')$. Both generalizations allow one to incorporate a time dependence of mean and noise strength during the proliferation. Assuming an absence of correlation between noise and neuron density prior to $t = 0$, the above steps lead to the generalized solution

$$\ln \rho(t) = \ln \rho_0 + \int_0^t \mu_{\text{rate}}(s) ds + \int_0^t \xi(s) ds. \tag{8}$$

Here, $\ln \rho(t)$ is still a Gaussian process, because it is a linear transformation of the Gaussian process $\xi(t)$. Due to the marginalization property of Gaussian processes, $\ln \rho(t)$ is normally distributed for any fixed time t with parameters

$$\mu(t) = \ln \rho_0 + \int_0^t \mu_{\text{rate}}(s) ds \qquad \text{and} \qquad \sigma^2(t) = \int_0^t \int_0^t C_\xi(s, s') ds ds'. \tag{9}$$

Thus, $\rho(t)$ is lognormally distributed with parameters $\mu(t)$ and $\sigma^2(t)$ specified in equation (9). Note that in equation (9), in contrast to equation (7), $\mu(t)$ and $\sigma^2(t)$ do not necessarily grow linearly with time but may exhibit a more intricate temporal dependence. Nonetheless, equation (9) predicts that $\mu(t)$ and $\sigma^2(t)$ are related through the proliferation time.

bioRxiv preprint doi: https://doi.org/10.1101/2022.03.17.480842; this version posted March 19, 2022. The copyright holder for this preprint (which was not certified by peer review) is the author/funder, who has granted bioRxiv a license to display the preprint in perpetuity. It is made available under aCC-BY 4.0 International license.

Supplementary tables

Table S1: Cortical areas included in this study.

Species	Area abbreviations
Mouse	FRP, MOp, MOs, SSp, SS-n, SSp-bfd, SSp-ll, SSp-m, SSp-ul, SS-tr, SSs, VISC, AUDd, AUDp, AUDpo, AUDv, VISal, VISam, VISl, VISp, VISpl, VISpm, ACAd, ACAv, ACAv, ACAv, ORBl, ORBm, ORBvl, AId, AIp, AIv, RSPagl, RSPd, RSPv, AONd, AONe, AONl, AONm, AONpv, TTd, TTv
Marmoset	A10, A9, A46V, A46D, A8aD, A8b, A8aV, A47L, A47M, A45, A47O, ProM, A11, A13b, A13a, A13L, A13M, OPAl, OPro, Gu, A32, A32V, A14R, A14C, A25, A24a, A24b, A24c, A24d, A6DR, A6Vb, A6Va, A8C, A6M, A6DC, A4c, A4ab, PaIM, AI, PaIL, DI, GI, IPro, TPro, S2PR, A3a, S2PV, A3b, S2I, S2E, A1-2, AuRTL, AuRT, AuRPB, AuRTM, AuR, AuRM, AuAL, AuA1, AuCM, AuCPB, AuML, AuCL, TPPro, STR, TE1, TPO, ReI, TE2, PGa-IPa, TPt, TE3, TEO, Pir, APir, Ent, A36, A35, TF, TL, TH, TLO, TFO, A23c, A23a, A29d, A30, A23b, A29a-c, A23V, ProSt, PF, PE, PFG, A31, AIP, PG, PEC, VIP, LIP, PGM, V6A, OPt, MIP, MST, FST, V5, V4T, A19M, V3A, V4, V6, A19DI, V3, V2, V1
Macaque_1	2, 5, 9, 10, 11, 12, 13, 14, 23, 25, 32, 24a, 24c, 24d, 46d, 46v, 7A, 7B, 7m, 8B, 8l, 8m, 8r, 9-46d, 9-46v, DP, ENTO, F1, F2, F3, F4, F5, F6, F7, LIP, MT, OPAI, OPRO, PERI, STPi, TEad, TEav, TEO, TH-TF, V1, V2, V3A, V4
Human	FA, FB, FC, FCBm, FD, FDΔ, FDt, FE, FF, FG, FH, FJ, FK, FL, FM, FN, LA1, LA2, LC1, LC2, LC3, LD, LE1, LE2, IA, IB, OA, OB, OC, PA, PB1, PB2, PC, PD, PE, PF, PG, PH, HA, HB, HC, HD, HE, HF, TA, TB, TC, TD, TE, TF, TG
Galago_1 & Owl Monkey	V1, V2, dV3, vV3, S1, M1, A1, MT, premotor, DL, Remain Ctx, Surr Ctx

bioRxiv preprint doi: https://doi.org/10.1101/2022.03.17.480842; this version posted March 19, 2022. The copyright holder for this preprint (which was not certified by peer review) is the author/funder, who has granted bioRxiv a license to display the preprint in perpetuity. It is made available under aCC-BY 4.0 International license.

Table S2: Results of the Shapiro-Wilk test for normality of $\ln(\rho_s)$ in marmoset cortical areas. Values rounded to two significant digits.

Area	S	p-value	Area	S	p-value	Area	S	p-value
V1	0.97	0.39	AI	0.95	0.0043	TH	0.97	0.66
A10	0.95	0.19	PaIL	0.95	0.33	TLO	0.96	0.18
A9	0.98	0.51	DI	0.97	0.098	TFO	0.97	0.26
A46V	0.98	0.56	GI	0.97	0.67	A23c	0.97	0.36
A46D	0.98	0.49	Ipro	0.97	0.66	A23a	0.99	0.98
A8aD	0.97	0.34	TPro	0.97	0.77	A29d	0.95	0.21
A8b	0.96	0.16	S2PR	0.92	0.006	A30	0.98	0.73
A8aV	0.96	0.17	A3a	0.95	0.04	A23b	0.97	0.45
A47L	0.96	0.052	S2PV	0.93	0.014	A29a-c	0.97	0.70
A47M	0.97	0.30	A3b	0.96	0.20	A23V	0.96	0.15
A45	0.96	0.18	S2I	0.97	0.33	ProSt	0.93	0.018
A47O	0.98	0.70	S2E	0.94	0.0046	PF	0.94	0.00083
ProM	0.97	0.21	Area1-2	0.97	0.37	PE	0.94	0.00065
A11	0.97	0.41	AuRTL	0.97	0.40	PFG	0.92	0.0046
A13b	0.96	0.58	AuRT	0.97	0.031	A31	0.97	0.31
A13a	0.91	0.048	AuRPB	0.98	0.89	AIP	0.96	0.063
A13L	0.97	0.45	AuRTM	0.97	0.73	PG	0.99	0.37
A13M	0.99	0.97	AuR	0.98	0.0093	PEC	0.91	0.0032
OPAl	0.99	0.99	AuRM	0.9	0.017	VIP	0.92	0.0044
OPro	0.98	0.75	AuAL	0.94	0.12	LIP	0.95	0.042
GU	0.95	0.058	AuA1	0.98	0.48	PGM	0.98	0.78
A32	0.97	0.20	AuCM	0.97	0.33	V6A	0.95	0.068
A32V	0.96	0.51	AuCPB	0.93	0.037	OPt	0.91	0.0015
A14R	0.98	0.77	AuML	0.97	0.44	MIP	0.9	0.00091
A14C	0.79	5.5e-06	AuCL	0.94	0.045	MST	0.98	0.53
A25	0.89	0.022	TPPro	0.98	0.91	FST	0.95	0.10
A24a	0.96	0.35	STR	0.96	0.44	V5	0.98	0.68
A24b	0.97	0.41	TE1	0.96	0.17	V4T	0.95	0.082
A24c	0.97	0.54	TPO	0.97	0.31	A19M	0.98	0.80
A24d	0.92	0.017	ReI	0.95	0.40	V3A	0.91	0.006
A6DR	0.97	0.23	TE2	0.96	0.15	V4	0.97	0.064
A6Vb	0.97	0.32	PGa/IPa	0.97	0.45	V6	0.96	0.017
A6Va	0.98	0.56	TPt	0.94	0.033	A19DI	0.95	0.074
A8C	0.95	0.055	TE3	0.93	0.026	V3	0.95	0.0076
A6M	0.99	0.98	TEO	0.95	0.087	V2	0.96	0.29
A6DC	0.91	0.002	A36	0.98	0.54	Ent	0.99	0.99
A4c	0.97	0.43	A35	0.97	0.31	APir	0.94	0.24
A4ab	0.96	0.076	TF	0.96	0.021	Pir	0.97	0.53
PaIM	0.93	0.20	TL	0.98	0.084			

bioRxiv preprint doi: https://doi.org/10.1101/2022.03.17.480842; this version posted March 19, 2022. The copyright holder for this preprint (which was not certified by peer review) is the author/funder, who has granted bioRxiv a license to display the preprint in perpetuity. It is made available under aCC-BY 4.0 International license.

Supplementary figures

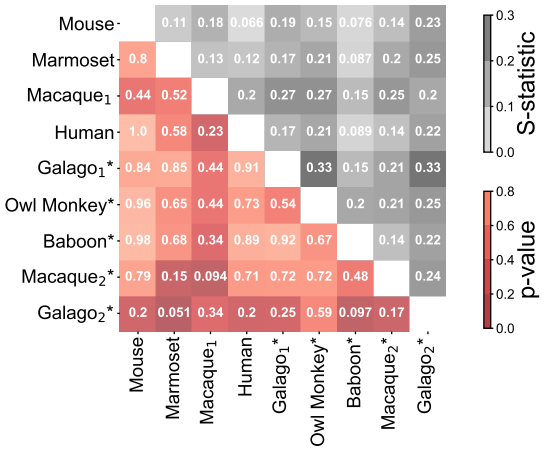

Figure S1: The z-scored log neuron density distributions of the four species are statistically indistinguishable at the 0.05 level based on pairwise Kolmogorov-Smirnov two-sample two-sided tests. P-values and S-statistics displayed below and above the diagonal, respectively.

bioRxiv preprint doi: https://doi.org/10.1101/2022.03.17.480842; this version posted March 19, 2022. The copyright holder for this preprint (which was not certified by peer review) is the author/funder, who has granted bioRxiv a license to display the preprint in perpetuity. It is made available under aCC-BY 4.0 International license.

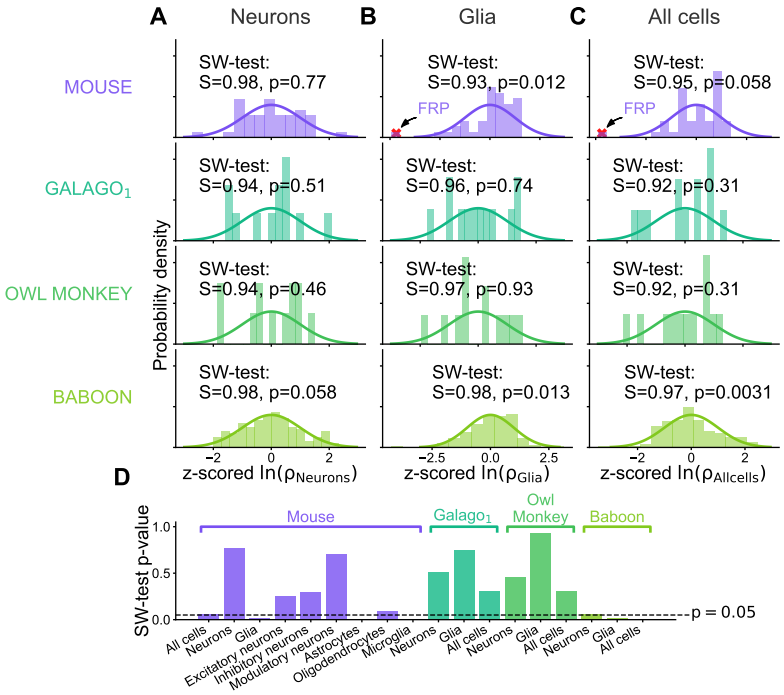

Figure S2: Comparison of neuron and glia lognormality. **A**–**C** Histogram of z-scored log density and result of Shapiro-Wilk test for neurons (**A**), glia (**B**), and all cells combined (**C**). **D** Barplot of p-values resulting from Shapiro-Wilk normality test for all cell types. Panel **A** is equivalent to the data shown in Figure 1.

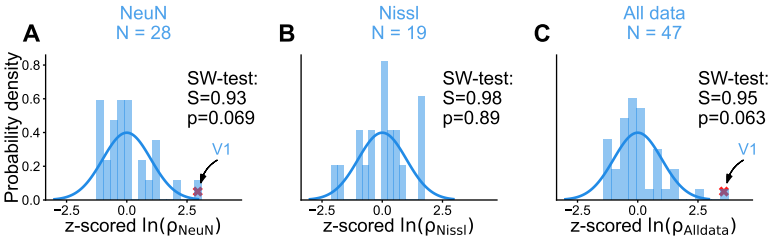

Figure S3: Lognormality of cell densities from different staining types in macaque cortex based on the macaque$_1$ data set. **A**-**C** Histogram of z-scored log density and result of Shapiro-Wilk test for NeuN staining only (**A**), Nissl staining only (**B**) and all measurements combined (**C**). The Nissl data were scaled down based on the linear relationship with the NeuN data [10]. Red crosses indicate outliers ($|\text{z-scored } \ln(\rho)| \geq 3$, which were excluded from the test. Panel **C** is equivalent to the data shown in Figure 1.

bioRxiv preprint doi: https://doi.org/10.1101/2022.03.17.480842; this version posted March 19, 2022. The copyright holder for this preprint (which was not certified by peer review) is the author/funder, who has granted bioRxiv a license to display the preprint in perpetuity. It is made available under aCC-BY 4.0 International license.

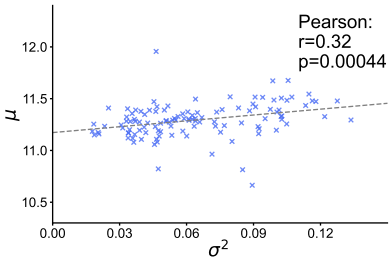

Figure S4: Neuron densities in the marmoset are compatible with our model of progenitor cell division with variability. μ and σ^2 are the mean and variance of $\ln(\rho)$, respectively; and are significantly correlated with each other, as predicted by the model.

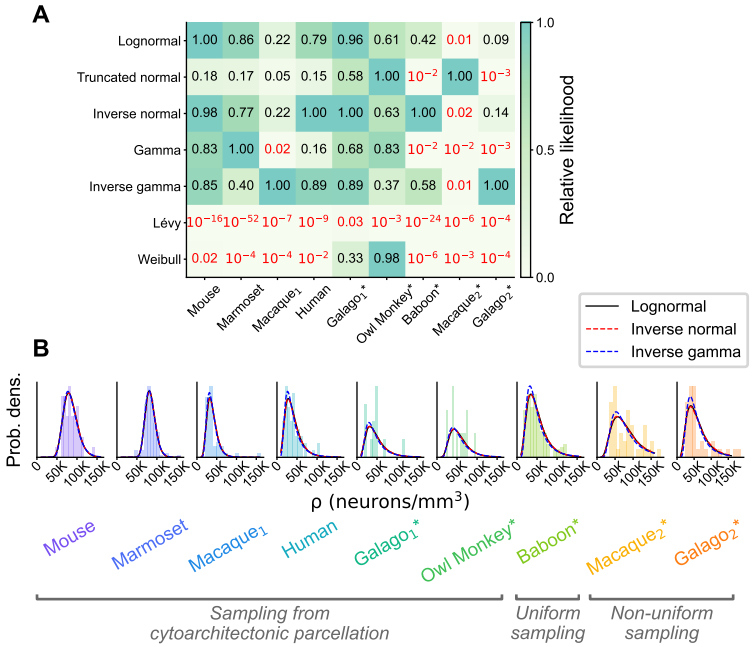

Figure S5: Statistical model comparison across the entire cortex of different animals. **A** Relative likelihood for seven compatible statistical models for all available area-level neuron density data sets; numerical values indicated for each model and animal. The red color indicates a relative likelihood < 0.05 with respect to the model with the highest likelihood. **B** The three best statistical models (according to the relative likelihood) fitted to the neuron density histograms in each animal; the three models produce visually nearly indistinguishable fits.

bioRxiv preprint doi: https://doi.org/10.1101/2022.03.17.480842; this version posted March 19, 2022. The copyright holder for this preprint (which was not certified by peer review) is the author/funder, who has granted bioRxiv a license to display the preprint in perpetuity. It is made available under aCC-BY 4.0 International license.

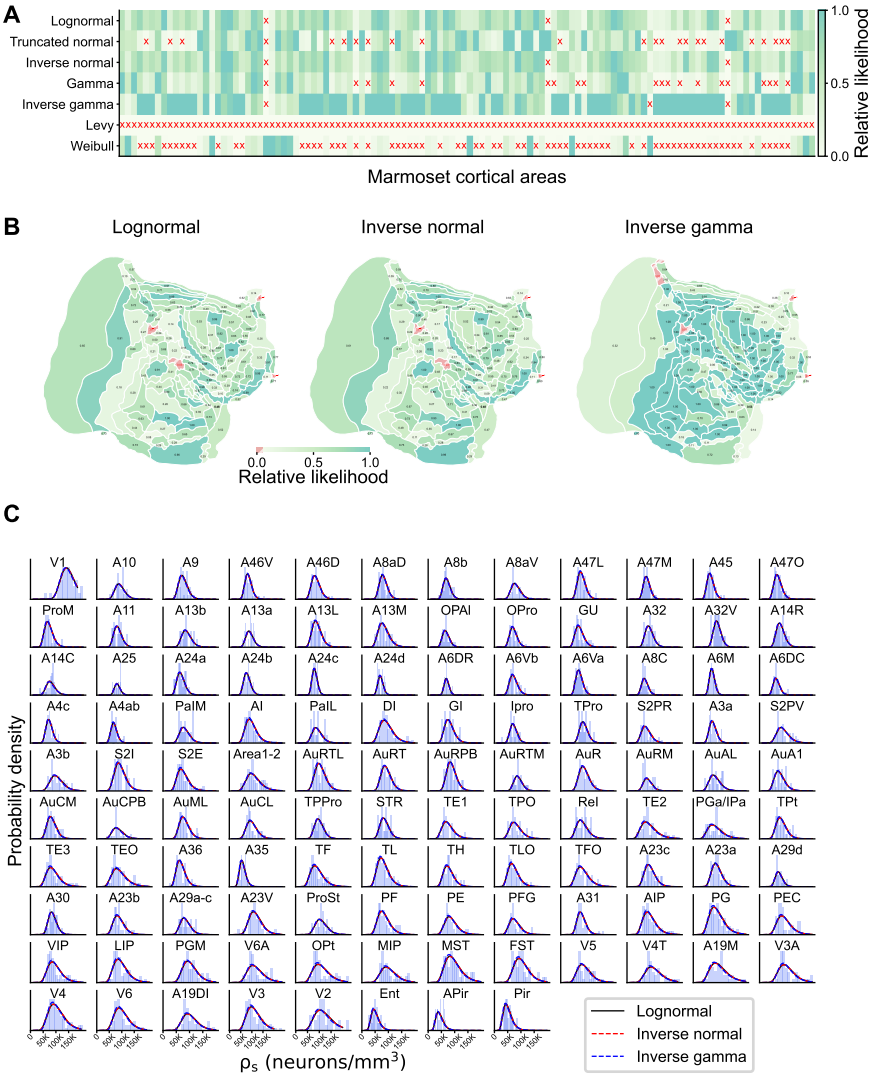

Figure S6: Statistical model comparison within the marmoset cortical areas. **A** Relative likelihood for seven compatible statistical models for all areas of the marmoset; a red cross (x) indicates a relative likelihood < 0.05 with respect to the model with the highest likelihood. **B** Spatial distribution of relative likelihood for the three best statistical models. **C** The three best statistical models fitted to the neuron density histograms in each area of marmoset cortex; the three models produce visually nearly indistinguishable fits.